Synchrotron *In-Situ* Aging Study and Correlations to the γ' Phase Instabilities in a High-Refractory Content γ-γ' Ni-Base Superalloy

STOICHKO ANTONOV, EUGENE SUN, and SAMMY TIN

Detailed *ex-situ* electron microscopy and atom probe tomography (APT) were combined with *in-situ* synchrotron diffraction to systematically quantify the chemical, morphological, and lattice instabilities that occur during aging of a polycrystalline high-refractory content Ni-base superalloy. The morphological changes and splitting phenomenon associated with the secondary γ' precipitates were related to a combination of discrete chemical composition variations at the secondary γ'/γ interfaces and additional chemical energy arising from γ precipitates that form within the secondary γ' particles. The compositional phase inhomogeneities led to the precipitation of finely dispersed tertiary γ' particles within the γ matrix and secondary γ particles within the secondary γ' precipitates, which, along with surface grooving of the secondary γ' particles, likely due to a spike in the lattice misfit at the particle interfaces, contributed to the splitting of the precipitates during aging.

https://doi.org/10.1007/s11661-018-4683-3

I. INTRODUCTION

NICKEL-BASE superalloys possess a unique combination of high strength and superb fatigue resistance even when exposed to high stress levels at elevated temperatures and corrosive environments.[1–3] These properties make them the ideal material for high-temperature components in the modern gas turbine engines and even power generation applications. The excellent properties can be largely attributed to a distinctive microstructure that consists of ordered ($L1_2$) intermetallic precipitates, namely, γ' (Ni_3Al), that are distributed within a disordered fcc (A1) matrix, namely, γ (Ni).[4–6] These precipitates restrict dislocation motion during plastic deformation due to their ordered and coherent nature.[7] In modern polycrystalline Ni-base superalloys, Al, Ti, Nb, and Ta are used as γ' forming elements in order to produce an optimized volume fraction of the γ' strengthening phase, while additions of refractory alloying elements, such as W, Mo, Cr, and Co, strengthen the γ matrix phase *via* solid solution strengthening.[8] Trace elements are further added to the mix to strengthen the grain boundaries and promote stable carbide and boride precipitation.[9] Even though the strength of the alloy and the temperature capability can be slightly improved with an increased γ' precipitate volume fraction, this tends to increase the overall alloy cost, due to increased difficulty in material manufacture, and to reduce alloy stability or environmental resistance.[10]

With the evolving powder-processing technology, which allows for the fabrication of more homogeneous alloys with higher refractory contents, new classes of powder-processed Ni-base superalloys have also been developed. The increases in the overall alloying additions in the material can have a significant impact on the microstructure of the alloy, which directly affects the mechanical properties. Hence, the levels of the refractory element additions need to be carefully optimized.[11] At relatively low concentrations, Ta, Nb, or Ti will preferentially partition to the γ' phase, which will cause an increase in the solid solution strengthening of the precipitate and increase the antiphase boundary (APB) energy, leading to an increase in the precipitate's resistance to deformation.[12] However, as the Ta and Ti content increases and the precipitate transitions to a Ta- or Ti-rich phase, the APB energy starts to decrease.[13] On the other hand, elevated concentrations of these γ' forming elements, near the alloy's solubility limits, may remain in solution within the γ phase and serve as solid solution strengthening additions.[14,15] This effect may be exploited through careful design optimizations and used to improve the strength and the high-temperature capabilities of the alloy.

STOICHKO ANTONOV is with the State Key Laboratory for Advanced Metals and Materials, University of Science and Technology Beijing, Beijing 100083, China. Contact e-mail: santonov@iit.edu EUGENE SUN is with the Rolls-Royce Corporation, Indianapolis, IN 46241. SAMMY TIN is with the Department of Mechanical, Materials, and Aerospace Engineering, Illinois Institute of Technology, Chicago, IL 60616.

Manuscript submitted March 20, 2018.

Surpassing the solubility limits of Nb, Ta, and Ti, however, can promote the formation of undesirable intermetallic phases, *e.g.*, δ (Ni_3Nb) or η (Ni_6AlNb), which are brittle and result in severe mechanical property deterioration.[16–20] In many cases, the high-refractory alloying content contributes to reducing the overall atomic mobility of the system and makes it difficult to attain a stable microstructure when conventional thermal-mechanical processing techniques are employed. This is a major drawback for alloy manufacturers, as the longer homogenization times required to equilibrate the material can significantly increase production costs. Furthermore, diffusion-controlled processes, such as precipitate coarsening, can deviate from classical models, making it harder to design alloys based on an integrated computational materials engineering (ICME) approach.

For binary Ni-Al alloy systems, γ' precipitate coarsening is governed by the minimization of surface energies and is consistent with the Oswald ripening theory,[21] which can be expressed by the Lifshitz and Slyozof[22] and Wagner[23] (LSW) equation and modified by Ardell.[24] In complex γ-γ' Ni alloy systems, however, the γ' precipitate evolution behavior may deviate from classical coarsening. In some instances, inverse coarsening takes place, where smaller precipitates grow at the expense of larger neighbors due to the elastic fields.[25] Another phenomenon is particle splitting, where the cuboidal precipitates will grow to a critical size and split into two or eight smaller particles.[26,27] Elasticity-based calculations have shown that the system energy decreases if the precipitate changes from a cube morphology to an octet.[28] Even though the splitting increases the overall surface energy in the system, various studies claim that the increase in surface energy is compensated by the decrease in elastic strain energy, as the misfit between γ and γ' decreases.[26,27,29] Other studies have reported that the observed morphological instabilities form as a result of reprecipitation of the γ matrix phase at the center of the γ' precipitate during aging and that the splitting is chemically driven.[30,31] Phase field modeling by Cha *et al.* suggests that the splitting is mediated by interface instability, caused by a concentration of strain energy around a concave particle wall, which promoted dissolution and interface grooving toward the center of the precipitate.[25] Finally, Mitchell *et al.* showed that the cooling rate of the alloy from the solutionizing temperature has a significant effect on the lattice misfit and, consequently, on the precipitate morphology and coarsening behavior.[32–35] Slow cooling rates of alloys, such as Udimet 720, follow classical LSW coarsening, while faster cooling rates result in higher elastic strains and complex precipitate morphologies.[33] In addition, fast cooling rates and Ta presence in alloys such as RR1000, result in cyclic particle splitting, due to a cyclic evolution of the unconstrained lattice misfit.[35] They speculate that the variation in the misfit behavior is associated with variations in the phase chemistry of the matrix and precipitates, as slow diffusing elements, such as Ta, would remain in supersaturation during γ' formation at cooling rates, effectively increasing the γ lattice parameter.

Understanding the fundamental effects associated with having an elevated concentration of refractory alloying elements in Ni-base superalloys will contribute to optimization of both chemistry and thermal processes. This knowledge can then be applied to engineer alloys and microstructures with greater temperature capability. Different aspects of the RRHT alloy series have been studied in detail. The higher nominal Nb content in the alloys leads to a higher level of solid solution of Nb in the γ phase, effectively increasing the strength of the matrix[16] and affecting the segregation behavior of B, by increasing its solubility in the matrix.[36,37] The effect of long-term heat exposure at 800 °C on the secondary phase formation can be found in Reference 20, while the effect of Hf additions on the MC carbide size, morphology, and number density can be found in Reference 38. In this work, the microstructural and compositional changes occurring in a high-refractory content Ni-base superalloy were quantified as a function of aging time at 1123 K (850 °C). *In-situ* synchrotron X-ray diffraction measurements of the changes in lattice parameter and misfit as a function of time at 850 °C were performed. These were complemented with detailed *ex-situ* microstructural studies using atom probe tomography (APT) and a field-emission scanning electron microscope (FESEM) at various aging times to quantify and explain the morphological changes occurring within the γ' precipitates. Thermodynamic predictions of phase fractions and chemistries, using Thermo-Calc, were used along with the results from the APT studies. Additionally, the formation and stability of secondary γ particles forming within the γ' precipitates were documented and studied as a part of this investigation.

II. EXPERIMENTAL PROCEDURE

An experimental, powder-processed Ni-base superalloy, RRHT1, was used in this investigation (Table I). Argon gas-atomized powders were sieved, canned, and consolidated by hot isostatic pressing, and subsequently, the billet was isothermally forged at ~ 1373 K (~ 1100 °C) and solution heat treated at 1443 K (1170 °C) for 1 hour. The material was control cooled from the solutionizing temperature at a rate of 1 K/s (1 °C/s), which is typical of large-scale industrial disk forgings. Samples were then cut from the bulk section of the forged pancake to avoid any surface heterogeneities, and aged at 1123 K (850 °C) for 1, 4, 16, 25, 50, 75, and 100 hours followed by air cooling. Samples for metallographic observation were prepared using standard grinding and polishing techniques down to a final polish of 0.06-μm colloidal silica. The γ' phase was preferentially dissolved by a solution of 33 pct HCL-33 pct NO_3-33 pct CH_3COOH-1 pct HF for ~ 8 seconds, and microstructural observations were performed using secondary electrons (SEs) in a JEOL* JSM 6701-F

---

*JEOL is a trademark of Japan Electron Optics Ltd., Tokyo.

Table I. Composition of RRHT1 (Atomic Percent)

Alloy	Cr	Al	Mo	Co	Nb	Ta	W	Ni
RRHT1	6 to 17	7.94	0 to 3	15 to 20	5.54	0.5 to 2.5	0.5 to 2.5	bal

FESEM, using an accelerating voltage of 10 kV. Multiple micrographs were taken at 20,000 times in different regions (across different grains) of each sample to obtain a statistically significant representation of the γ' phase and particle size distributions. In addition, higher magnification images, 80,000 times, were taken to observe the smaller nanoscale precipitates. All images were analyzed with ImageJ coupled with an in-house script for automated precipitate quantification, and considering 1900 to 3600 individual precipitates per sample.

Synchrotron diffraction samples measuring 1.2 mm × 1.2 mm × 50 mm were sectioned from the as-solutioned material and manually ground down to Φ0.9-mm needles with 4000-grit grinding paper. To prevent oxidation during the high-temperature aging, the needles were encapsulated in-between two Φ1-mm quartz tubes in an Ar-filled glovebox and sealed with wax. High-resolution synchrotron powder-diffraction data were collected using beamline 11-BM at the Advanced Photon Source in Argonne National Laboratory and an X-ray beam with an average wavelength of 0.413 Å. A three-axis translation stage held the sample and allowed it to be spun at ~ 5400 rpm (90 Hz) to reduce any preferred orientation effect. The analyzer system, 2θ arm, is comprised of 12 perfect Si (111) analyzers and 12 Oxford-Danfysik $LaCl_3$ scintillators, with a spacing of 2 deg 2θ.[39] The discrete detectors covering an angular range from 4 to 20 deg 2θ were scanned over a 38 deg 2θ range, with a step size of 0.002 deg 2θ and scan speed of 0.01 deg/s, resulting in a scan duration of 14.6 minutes. Data were collected while continually scanning the diffractometer 2θ arm. The instruments were calibrated using a mixture of NIST standard reference materials, Si (SRM 640c) and Al_2O_3 (SRM 676), where the lattice constant of the Si standard determines the wavelength for each detector. Corrections for detector sensitivity, 2θ zero offset, small differences in wavelength between detectors, and the source intensity, as noted by the ion chamber, are applied.[39] The 12 individual data sets were then merged into a single set of intensities evenly spaced over 2θ. A diffraction pattern was collected prior to the start of aging to ensure the alignment of the sample and hot gas heating system. The samples were then brought up to the aging temperature, 1123 K (850 °C), using a Cyberstar Hot Gas Blower, which has been calibrated as a function of temperature using the known thermal expansion coefficients of Al_2O_3 for the *a* and *c* unit cell parameters. Typically, the temperature equalization zone is ± 5 K (± 5 °C) for a region of 0.8 mm, the thickness of the X-ray beam. The duration of the *in-situ* aging study was 23.4 hours.

III. RESULTS

The micrographs in Figure 1 show the representative microstructure of the RRHT1 alloy as a function of aging time at 1123 K (850 °C) for up to 100 hours. Starting from the as-solutioned condition, *i.e.*, 0 hours, up to aging for 16 hours, the γ' precipitates exhibit normal coarsening behavior and the γ' precipitates evolve from being initially near spherical to possessing a dendriticlike morphology. After aging at 1123 K (850 °C) for 25 hours, the γ' precipitates are smaller and cuboidal, suggesting that precipitate splitting had occurred. This microstructure was homogeneous throughout the sample, where only a few unsplit (larger) precipitates can be observed, usually in the vicinity of the grain boundary. After further aging, 50 hours at 1123 K (850 °C), the precipitates do not appear to have coarsened significantly when compared to the 25-hours aging time. Thermal exposure for 75 and 100 hours shows that the precipitates have coarsened and split again, respectively; however, they have maintained the cuboidal morphology. Looking at the average equivalent diameter (Figure 1), the precipitates coarsen from ~ 150 nm, in the as-solutioned state, to ~ 167 nm after 16 hours of aging. After the 25-hours exposure, the split precipitate size is ~ 140 nm and starts to coarsen again up to ~ 197 nm, after 75 hours of aging. After another splitting, after 100 hours at 1173 K (850 °C), the precipitate size is ~ 160 nm. It should be noted that error bars for the average equivalent diameter plot in Figure 1 represent the precipitate size spread rather than the area-to-area deviation. The area fraction of the γ' phase increases from ~ 38 pct, in the as-solutioned condition, to ~ 41 pct after the first hour of aging and remains relatively constant up to the first splitting event after 25 hours. Subsequently, as the precipitates start to coarsen again, the area fraction increases to ~ 45 pct and again remains relatively constant up to 100 hours. It is important to note that the equivalent diameter and area fraction are most accurate when the precipitates have a regular spherical or cuboidal shape; however, errors are introduced as the precipitate transitions to a more irregular morphology. In addition to the secondary γ' precipitates, tertiary γ' particles also form and a high number density of particles can be observed in the 1-hour aged sample. Although these precipitates cannot be resolved in the as-solutioned sample, *i.e.*, 0 hours, previous APT results show that Al-rich clusters (precursors to tertiary γ' but uncertain whether they have an ordered $L1_2$ crystal structure at this point) form in the matrix, likely during cooling, in order to alleviate the supersaturation of the matrix.[40] Further aging, up to 4 hours at 1123 K (850 °C), results in coarsening, where

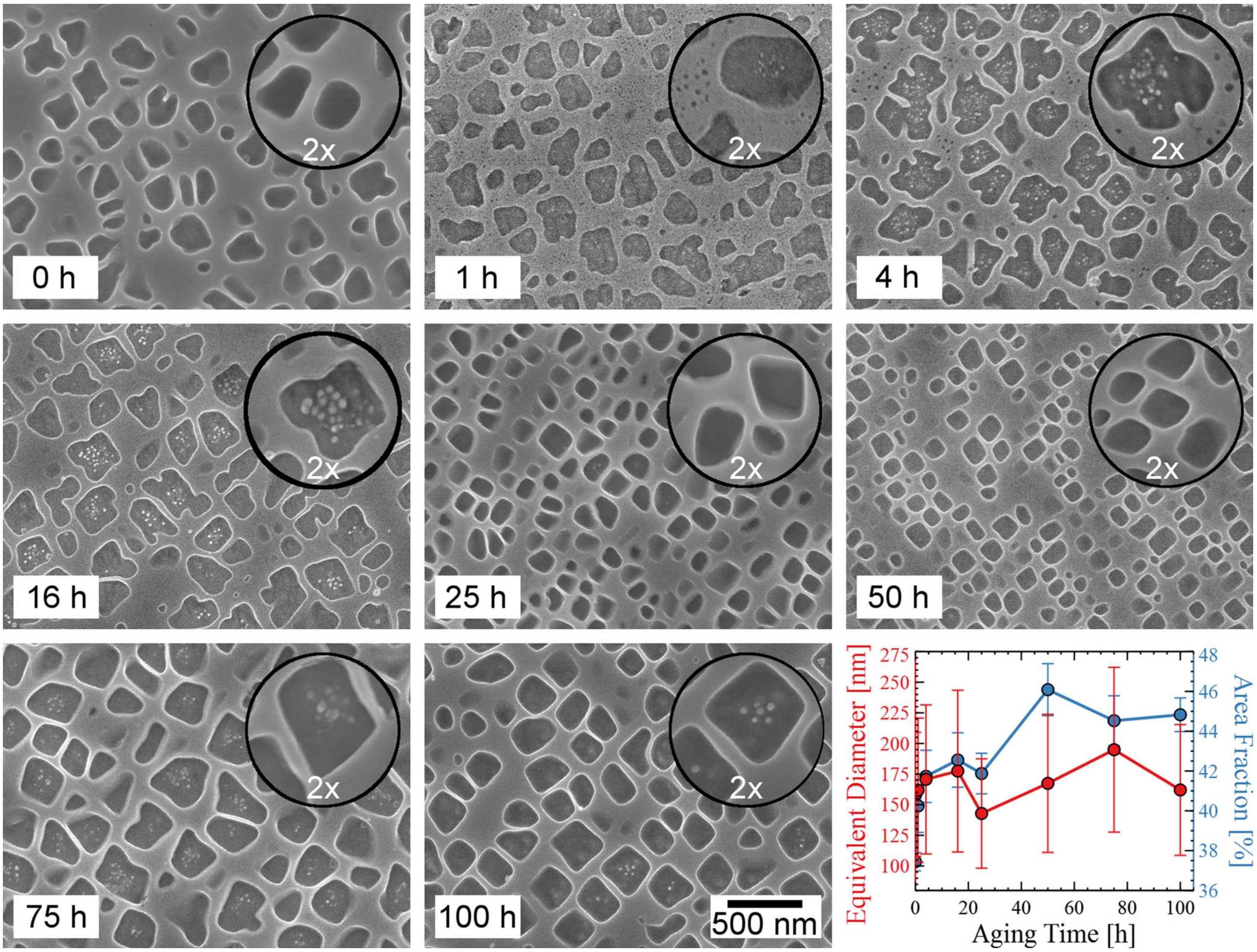

Fig. 1—Effects of aging time on the microstructure and the precipitate stability of alloy RRHT1 during aging at 1123 K (850 °C).

the number density has reduced, and finally, a complete resolution back into the matrix occurs between 4 and 16 hours. Finally, secondary γ precipitates are observed to form in the 1-hour sample—the white contrast precipitates in the insets of Figure 1 coarsen up to 16 hours of aging and disappear once the secondary γ' precipitates split. This transient phase reforms in most of the secondary γ' precipitates after 75 hours of aging; however, most of it redissolved after 100 hours at 1123 K (850 °C), when another splitting event occurred.

In our previous investigation, we reported the bulk phase chemistries, as averaged over many APT needles and precipitates, and noted that the phase composition of the matrix and the secondary γ' phase changes only slightly from 4 to 50 hours of aging.[40] Figure 2 shows the proximity histograms with respect to a 14 at. pct Cr isoconcentration surface of a randomly selected γ/γ' interface for the three aging conditions: as solutioned, and 4 and 50 hours at 1123 K (850 °C). Cr and Co buildup and Al, Nb, and Ni depletion can be observed in the matrix phase toward the interface for the as-solutioned condition, while Nb enrichment and Ta and Cr depletion can be seen in the γ' phase. At the interface itself, some Ni, Mo, W, and B segregation can be observed. After 4 hours of aging at 1123 K (850 °C), the gradients in the concentration profiles in the γ' phase have flattened out, but some elemental gradients in the γ phase can still be observed, particularly for the Ni, Cr, Nb, and Al. After 50 hours of aging at 1123 K (850 °C), only slight gradient in the Ni and Cr in the γ phase can be observed. Overall, the elemental segregation to the interface remains the same, where Ni, Mo, W, and B are enriched and Cr is slightly depleted. It should be noted here that proxigrams of similar interfaces in the respective aging condition produced similar, if not identical, elemental concentrations; hence, these can be viewed as representative of the majority of the precipitates.

The compositions of the γ and γ' phases were obtained from the proxigrams in Figure 2 by averaging 4 nm away from the interface up to 20 nm into the phase, and the results are presented in Table II. These compositions are similar to the bulk compositions averaged over many samples and precipitates, as shown previously.[40] This data set is consistent and provides further evidence that the proxigrams in Figure 2 can be regarded as representative of the majority of precipitates. Overall, the γ' composition remains relatively constant from 0 to 50 hours, although slight saturation of Cr and Co exists in the as-solutioned state, which likely drives the precipitation of the secondary γ phase. Similarly, the γ

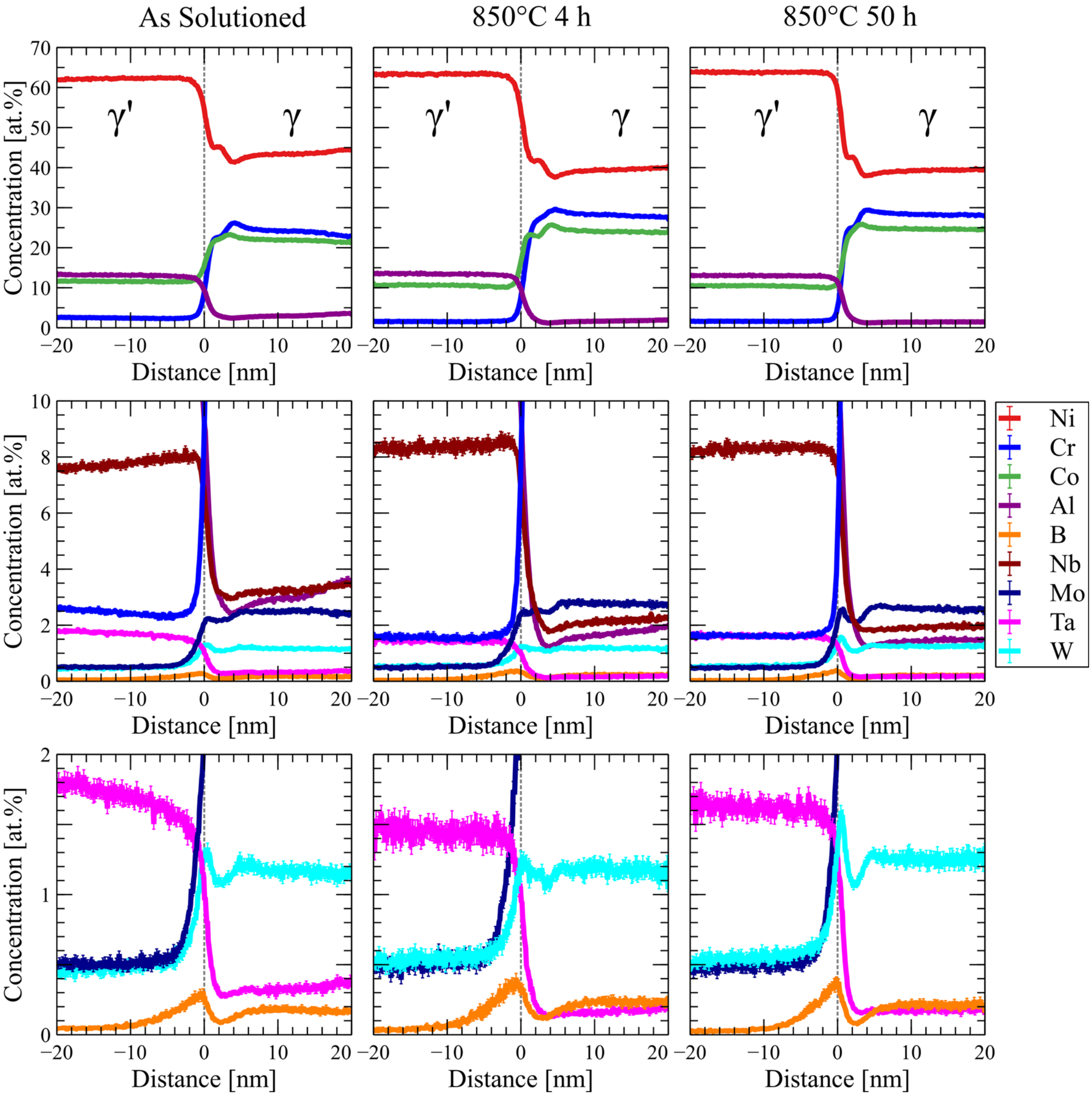

Fig. 2—Proximity histograms with respect to a 14 at. pct Cr isoconcentration surface for the as-solutioned, 4, and 50 h samples.

Table II. Phase Compositions at Different Aging Heat Treatments (Atomic Percent)

Phase	γ'				γ			
Aging Time (h)	As Solutioned	850 °C, 4 h	850 °C, 50 h	JMatPro 850 °C	As Solutioned	850 °C, 4 h	850 °C, 50 h	JMatPro 850 °C
Ni	62.21 ± 0.19	63.35 ± 0.24	63.62 ± 0.17	63.1	43.68 ± 0.41	39.56 ± 0.29	39.52 ± 0.20	34.7
Cr	2.46 ± 0.10	1.56 ± 0.06	1.97 ± 0.04	1.9	23.80 ± 0.50	28.02 ± 0.29	28.26 ± 0.17	30.1
Al	13.16 ± 0.13	13.47 ± 0.16	12.77 ± 0.11	13.3	3.15 ± 0.24	1.75 ± 0.11	1.28 ± 0.04	1.6
Mo	0.51 ± 0.02	0.51 ± 0.04	0.48 ± 0.02	0.27	2.48 ± 0.06	2.76 ± 0.05	2.47 ± 0.05	2.7
B	0.07 ± 0.03	0.06 ± 0.04	0.03 ± 0.03	0	0.17 ± 0.01	0.23 ± 0.01	0.21 ± 0.01	0
Co	11.59 ± 0.11	10.63 ± 0.16	10.49 ± 0.11	10.3	21.75 ± 0.23	23.98 ± 0.18	24.65 ± 0.15	28.5
Nb	7.73 ± 0.13	8.34 ± 0.13	8.38 ± 0.12	8.9	3.30 ± 0.11	2.16 ± 0.09	1.93 ± 0.05	0.99
Ta	1.72 ± 0.06	1.45 ± 0.05	1.62 ± 0.04	1.72	0.34 ± 0.03	0.17 ± 0.02	0.18 ± 0.01	0.07
W	0.47 ± 0.03	0.54 ± 0.03	0.57 ± 0.03	0.44	1.16 ± 0.03	1.18 ± 0.04	1.33 ± 0.03	1.24

phase is saturated with γ' forming elements in the as-solutioned state; however, it is relatively constant throughout the aging period. It is interesting to note that the B concentration in the γ matrix is rather high, ~ 0.2 at. pct, when compared to similar Ni-base superalloys, but it is consistent with the reports of high B concentration in the other high Nb-content superalloys.[36,37] Finally, γ and γ' phase compositions, as predicted by JMatPro, which uses the TTNi8 database, have been added to Table II. Overall, there is good agreement between the observed experimental compositions after 50 hours at 1123 K (850 °C) and the predicted equilibrium phase chemistries, which is consistent with the observations made using the predicted results by Thermo-Calc with TCNi8 in Reference 40. The largest discrepancy appears to be in the underestimation of the partitioning of the γ' phase formatting elements, Nb and Ta, to the γ phase, consistent with other reports.[51]

To understand the influence of the lattice misfit on the precipitate instability, the obtained APT phase chemistries were used along with Vegard's relation, Eq. [1], and published Vegard coefficients,[41] to estimate the unconstrained γ and γ' lattice parameters as

$$\begin{aligned} a_{\gamma} &= a_0^{\gamma} + \sum_i \Gamma_i^{\gamma} x_i^{\gamma} \\ a_{\gamma'} &= a_0^{\gamma'} + \sum_i \Gamma_i^{\gamma'} x_i^{\gamma'} \end{aligned} \qquad [1]$$

where a_{γ} and $a_{\gamma'}$ are the calculated lattice parameters for γ and γ', respectively. a_0^{γ} and $a_0^{\gamma'}$ are the lattice parameters for pure Ni and Ni_3Al[42]; Γ_i^{γ} and $\Gamma_i^{\gamma'}$ are the Vegard coefficients for element i; and x_i^{γ} and $x_i^{\gamma'}$ are the concentrations of element i for γ and γ', respectively. The lattice misfit, δ, was calculated using Eq. [2]:

$$\delta = 2\frac{a_{\gamma'} - a_{\gamma}}{a_{\gamma'} + a_{\gamma}} \qquad [2]$$

The constrained lattice misfit, δ, represents the coherency strain between the γ and γ' phases and is the sum of the unconstrained lattice parameters (function purely of the phase chemistry) and the elastic strain associated with conforming to the coherency of the interface, as well as any difference in the coefficient of thermal expansion (negligible for Ni and Ni_3Al). Note that using Eq. [2] with the parameters calculated by Eq. [1] will approximate an unconstrained misfit, ε. This can be related back to the constrained misfit by elasticity theory, and approximates to Reference 43

$$\varepsilon = \frac{3}{2}\delta \qquad [3]$$

Calculations of the lattice parameters and misfit for RRHT1 were carried out using the compositions in Reference 40. The misfit in RRHT1 was found to increase from ~ 0.2 pct in the as-solutioned state to ~ 0.5 pct in the 4-hours aged condition, and finally ~ 0.6 pct in the 50-hours aged samples. These values are rather high, and a loss of coherency is expected to occur at ~ 0.5 pct, which shows the limitations of using such empirical estimations. To be fair, Vegard's relationships for lattice parameters are developed for binary and ternary systems; hence, extrapolating to the complex chemistries of modern superalloys introduces a certain degree of error. It should be noted that, as this is a positive misfit alloy, the lattice misfit is expected to become smaller at higher temperatures due to differences in the coefficients of thermal expansion in the γ and γ' phases. Additionally, lattice misfit calculations were carried out with JMatPro, and the results for 298 K and 1123 K (25 °C and 850 °C) are also compiled in Table III. Overall, the predicted lattice misfit has a modest difference of only ~ 0.1 pct in magnitude existing between the high- and low-temperature calculations, and is similar to the lattice misfit calculated based on the APT data. JMatPro calculates the lattice parameters based on the equilibrium thermodynamic calculations, coupled with databases of experimentally measured parameters and thermal expansion coefficients.[44]

Finally, a few representative scans of the *in-situ* diffraction are plotted in Figure 3(a). As expected, based on the APT data, the γ' lattice parameter changes only slightly, while the γ lattice parameter evolves to a higher degree. No sudden changes were observed that would correspond to a precipitate splitting phenomenon. Initially, Reitveld refinement of the full patterns was performed using GSAS-II, which uses crystallographic information files built with the APT data and an instrument parameter file to fit the experimental pattern using pseudo-Voight functions. As some of the γ peaks displayed a slight asymmetry, the final refinement was performed solely on the {222} peak. The reason for the γ peak abnormality is likely due to small distortions of the γ lattice due to the higher B content as interstitial atoms; however, further work is currently underway. It should be noted that no γ' superlattice peaks were observed, as the scattering factor appears to be too low; however, select conditions were also analyzed using neutron diffraction (not shown here), and the positive misfit and peak positions calculated with the neutron diffraction data are in good agreement with the synchrotron data. In addition, five minor reflections for the MC carbides were identified, and APT data from Reference 38 were used to build the crystallographic information files. The MC carbide phase is predicted to be less than 1 pct by Thermo-Calc.[40] Finally, no additional peaks corresponding to sample oxidation were observed. The

Table III. Calculated and Predicted Lattice Parameters and Misfit of RRHT1

Alloy	RRHT1 As Solutioned	RRHT1 Aged 4 h at 850 °C	RRHT1 Aged 50 h at 850 °C	JMatPro Predictions at 25 °C	JMatPro Predictions at 850 °C
γ Lattice (Angstrom)	3.607 ± 0.002	3.599 ± 0.002	3.596 ± 0.001	3.587	3.636
γ' Lattice (Angstrom)	3.616 ± 0.001	3.617 ± 0.001	3.617 ± 0.001	3.607	3.652
Misfit δ	0.23 pct	0.49 pct	0.60 pct	0.52 pct	0.42 pct
Unconstrained Misfit ε	0.15 pct	0.33 pct	0.40 pct	0.35 pct	0.28 pct

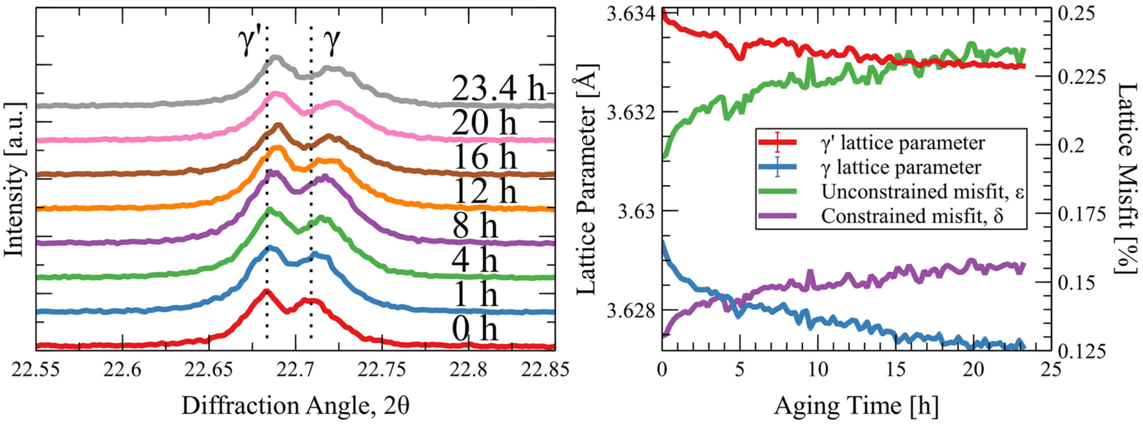

(a) **(b)**

Fig. 3—(*a*) Select diffraction patterns of the {222} peak at various times and (*b*) lattice parameters and misfits as a function of aging time calculated from the *in-situ* synchrotron experiments.

lattice parameters as a function of aging time, as determined from the refinement of the *in-situ* synchrotron experiments, are plotted in Figure 3(b), along with the lattice misfit, as calculated from Eqs. [2] and [3]. It should be noted that due to the impracticality of studying the unconstrained lattice parameters *in situ*, the unconstrained lattice misfit, ε, can only be approximated for the worst case using Eq. [3]. Overall, as the level of solute saturation in the γ and γ' phases decreases, the lattice parameters of the two phases also decrease, albeit more strongly in the γ than the γ' phase. Consequently, the lattice misfit between the two phases was observed to increase. Interestingly, the experimentally measured lattice parameters are much higher than the ones calculated from Eq. [1], and the lattice misfit is much smaller, ~ 0.15 and ~ 0.23 pct for the constrained and unconstrained cases, respectively, after 23.4 hours of aging. Surprisingly, no significant change in lattice parameters due to precipitates splitting can be observed in Figure 3. It should be noted that the tertiary γ' and secondary γ phases were not considered in the refinement, as these are a very small fraction of the phases and exist only for limited time. Furthermore, Collins *et al.* did not observe any peak intensity change for the formation of tertiary γ' and argue that they could be ignored in the analysis.[45]

IV. DISCUSSION

The morphological, compositional, and lattice evolution that occurs within the microstructure of a powder-processed, polycrystalline Ni-base superalloy with high-refractory content during aging at 1123 K (850 °C) was investigated. It should be noted that the cooling rate from the solutionizing temperature is relatively slow, ~ 1 K/s, which is suggested to result in classical LSW precipitate coarsening albeit with complex morphology, according to studies on RR1000 and Udimet 720.[33,35] Starting from the as-solutioned condition, the γ' precipitates evolve from exhibiting a dendrite-like morphology in the as-solutioned state to a more cuboidal morphology in the near-equilibrium state through the formation of transient phases, surface grooves, and finally cyclical particle splitting (Figure 1), which is typical for faster cooling rates.[35]

As previously mentioned, a minimization of the sum of the surface and elastic strain energies needs to be considered when dealing with a coarsening precipitate. The change in free energy of the precipitate can be calculated as[31]

$$\Delta G = \Delta E_{\text{surface}} + \Delta E_{\text{strain}} + \Delta E_{\text{interaction}} \qquad [4]$$

where $\Delta E_{\text{surface}}$, ΔE_{strain}, and $\Delta E_{\text{interaction}}$ are the change in surface, strain, and precipitate-matrix interaction energies, respectively. Typically, for most systems with coherent precipitates of small lattice misfits, the strain and interaction energies are negligible and the precipitates take on a spherical morphology, as a spherical shape has a minimum surface energy, given as

$$\Delta E_{\text{surface}} = \mathrm{SA}(r)\gamma \qquad [5]$$

where $\mathrm{SA}(r)$ is the surface area of a precipitate with radius r and γ is the interfacial energy density between the precipitate and the matrix.

As the precipitate coarsens and the volume increases with respect to the surface area, the strain and interaction energies become substantially higher and affect precipitate coarsening. Particularly, the morphology of the precipitates is highly dependent on the elastic strain energy, associated with the lattice misfit, as it varies with the habit plane, shape, and volume of the precipitates. In addition, it was found that the elastic energy of a monolithic precipitate is higher than a periodic distribution of precipitates with an equivalent total volume, as strong elastic interactions between neighboring γ' precipitates will influence the growth rate.[46] The elastic energy is highly dependent on the elastic anisotropy of the material, termed the "anisotropy factor" and expressed by[47]

$$K = c_{11} - c_{12} - 2c_{44} \qquad [6]$$

where c_{11}, c_{12}, and c_{14} are the elastic constants of the matrix or precipitate phase. Although these parameters are different for the γ and γ' phases in Ni-base superalloys, the elastic constant difference between the matrix and the precipitates can be neglected, as it has been shown that this contribution is small relative to driving force from the elastic strain energy.[48] Due to the negative anisotropy of Ni_3Al, it typically transitions from a sphere to cube defined by (100) planes as the volume becomes significantly larger with respect to the changes in surface area.[31,47] Khachaturian *et al.* performed a theoretical analysis of the strain-induced shape changes in cubic precipitates during coarsening based on microelasticity theory and derived the elastic energy, $\Delta E_{\text{strain}} + \Delta E_{\text{interaction}}$, relative to that of a thin plate:[47]

$$\Delta E^e = \alpha V E_1 \qquad [7]$$

where α is a shape factor based on two geometric integrals, V is the precipitate volume, and E_1 is the elastic energy density given as

$$E_1 = \frac{-\frac{1}{2}\beta^2 K \varepsilon^2}{c_{11}(2c_{11} - K)} \qquad [8]$$

where ε is the unconstrained lattice misfit and β is the bulk modulus, given by

$$\beta = c_{11} + 2c_{12} \qquad [9]$$

Using the elastic constants, interfacial energy density, and shape factor, α, given by Khachaturian *et al.*,[47] a critical morphology change radius *vs* elastic strain energy can be calculated for different morphological transformations, given in Figure 4. Looking at the misfits calculated from the *in-situ* experiments, an unconstrained lattice misfit of 0.23 pct would result in a spherical to cuboidal shape change above a 102-nm particle size; however, for a cube to doublet or octet transition, the critical radius is 353 or 649 nm, respectively. Referring to the sequence of microstructural images shown in Figure 1, the sphere to cube transition is likely occurring during aging. However, the precipitates were observed to reach a maximum of ~ 170 nm before splitting, which is far from the calculated critical splitting size. This suggests that there are other contributions driving the precipitate splitting phenomenon.

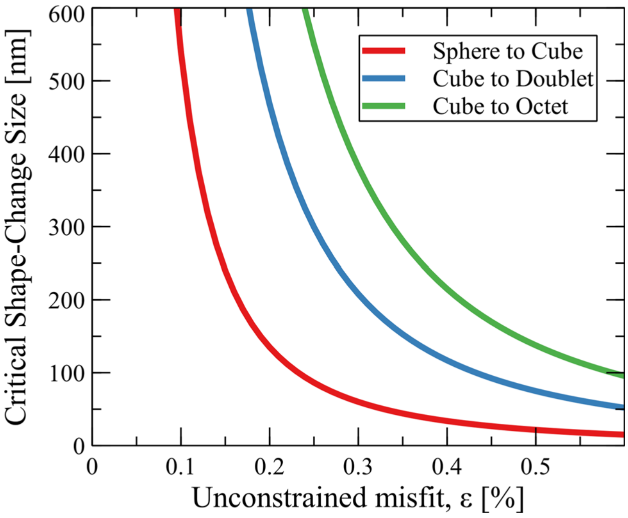

Fig. 4—Critical shape change radius *vs* unconstrained lattice misfit.

Although high-resolution transmission electron microscopy (HRTEM) techniques show the existence of elemental buildup at γ-γ' precipitate interfaces in RR1000,[49] other APT studies on the chemical evolution during aging of RR1000 show no such elemental segregation.[50] From the proxigrams in Figure 2, it is obvious that the composition of the γ and γ' adjacent to the interface is significantly different than the bulk composition of the phases. Lapington *et al.* observed a similar Cr plateau near the γ/γ' interface (looking at the proxigrams in the study, such a plateau can also be observed for the Ni and Co as well) and list field evaporation artifact as one of the possible reasons for it.[51] In RRHT1, chemical variation adjacent to the interface involves most of the elements and was confirmed to be surrounding the entire precipitate, rather than just the sides or corners. Considering this and the different evaporation conditions, it is unlikely that this is a field evaporation artifact, but rather a transient-type phase, which forms as γ' grows and rejects solutes. This seems to be inherent to the compositionally complex nature of these alloys; however, further studies are required to elucidate the true nature of this chemical variation. Using the proxigrams along with Eq. [1], it is possible to qualitatively map the variations in lattice parameter as a function of distance from the precipitate interface. Figure 5 shows the lattice parameter as a function of distance from the interface for the three aging conditions. Generally, the lattice parameters far away from the interface are as expected, where a longer aging time alleviates saturation and produces a more homogeneous and uniform elemental profile. This obviously leads to correspondingly invariant lattice parameter profiles. The γ' slightly increases from the as-solutioned sample but remains relatively unchanged upon aging from 4 to 50 hours. The lattice parameter of the matrix away from the interface, on the other hand, initially decreases and the profile flattens out, as the concentration gradient is decreased, and further decreases slightly from 4 to 50 hours. The most significant thing to note is the lattice parameter of the matrix close to the interface. Due to the elemental buildup and depletion adjacent to the interface, there is a lattice parameter dip in a region approximately ~ 5-nm wide adjacent to the phase boundary. This observation is similar to those reported in similar HRTEM studies, where a lattice parameter dip was reported for coarsened and unsplit precipitates but alleviated following the splitting.[49] This is not the case here, as the dip remains consistent for the 4-hour as well as the 50-hour aging times. This dip would cause a significant lattice parameter misfit increase at the interface of the precipitates, and as the volume fraction of the γ' phase is ~ 50 pct, it would result in a major contribution to the elastic strain energy. Cha *et al.* studied precipitate splitting *via* phase field modeling and found that, as the [111] direction growth becomes dominant due to a high chemical driving force, the precipitate sides become concave.[25]

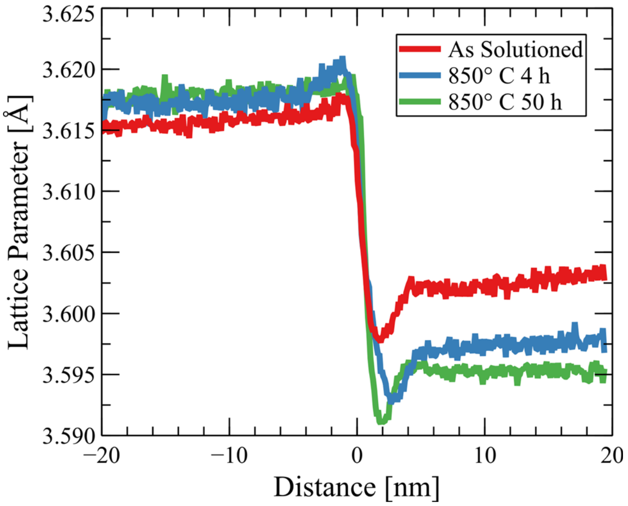

Fig. 5—Lattice parameter as a function of distance from the interface.

The elastic strain energy concentrates around the concave edge, which drives precipitate dissolution, and a surface groove forms, which is the precursor of splitting. From Figure 1, it is apparent that, prior to splitting, the precipitates assume a butterflylike morphology, with the cube corners protruding out, *i.e.*, growth in the [111] direction. Although it was observed in the three-dimensional reconstruction of the APT results that the elemental deviation at the matrix/precipitate interface is present around the precipitate, such a concentration of strain energy would cause grooving in the precipitate surface, which is in agreement with the precipitate morphologies for the 4 and 16 hours, prior to splitting. In Figure 1, it can be seen that such grooving is present at multiple locations along the precipitate interface in these samples. This surface instability, however, is present even after the particles have split and is not reduced by any amount. It is, therefore, likely a contributing factor to, but not the only feature driving, the splitting.

Doi *et al.*[31] and Vogel *et al.*[30] used dark-field TEM or APT to study γ precipitation in γ' precipitates in the Ni-Al-Ti system. Their calculations showed that, even though large surface area and interfacial energy were created through the precipitation of spherical γ precipitates, there was a local decrease in molar Gibbs free energy. Further aging caused the spherical γ precipitates to transform to plates due to an increase in elastic strain energy compared to interfacial energy. In that ternary system, individual γ precipitates connecting with the matrix drove the γ' splitting. The formation of γ precipitates can also be observed in the RRHT1; however, key differences exist from those formed in the simple ternary alloy system, likely due to the complexity of the alloy. These precipitates form cyclically, similar to the splitting phenomenon, where they redissolve when the precipitates split and remain only in large, unsplit precipitates. The compositions of the secondary γ precipitates are tabulated in Table IV, for the 4- and 50-hour samples. Comparing the compositions of the γ precipitates after 4-hour aging to the composition of the γ matrix (Table II), it is apparent that the Ni, Al, Mo, W, Nb, and W contents are depleted, whereas the Cr and Co contents are much higher. After 50 hours of aging, the composition of the γ precipitates is similar to that of the matrix and only a modestly higher Co concentration (from the γ forming elements) can be observed. The stability of γ phase inside the γ' can be evaluated with thermodynamic predictions based on the CALPHAD methodology, by evaluating the secondary γ' phase composition from the APT data. Ideally, the results should indicate that only the γ' phase is stable; however, this is not the case. The results in Figure 6 were calculated using Thermo-Calc and the TCNi8 database. A stable γ phase is predicted to form for all three samples, but the phase fraction decreases with aging time as the γ' precipitates tend toward equilibrium. As the secondary γ' precipitates form at higher temperatures, the solubility of Cr and Co is higher and a subsequent cooling to a lower temperature renders these elements in supersaturation. Chen *et al.* observed a similar behavior associated with Co in RR1000, where the Co concentration, initially supersaturated in the precipitate due to inadequate diffusion time, decreased as a function of splitting cycles and precipitate size.[49] The unsplit precipitates had a high Co concentration in the center, as compared to the outer regions, while the split precipitates were more homogeneous in terms of Co concentration. Although RR1000 does not form γ precipitates, the driving force behind their formation in the RRHT alloy is similar. With the majority of the γ' precipitates forming upon cooling from solution at temperatures just below the γ' solvus temperature, ~ 1423 K (1150 °C), Co and Cr solute atoms likely become "trapped" in the secondary γ' precipitates during cooling, as their solubility in the γ' phase decreases as a function of temperature. The combination of increasing diffusion distance and decreasing diffusivity causes the γ' phase in the as-solutioned microstructure to be supersaturated with Co and Cr solute. Upon aging, the thermal energy provides sufficient mobility to the trapped solute to alleviate the supersaturation. Similar to the γ precipitation in the Ni-Al-Ti system, formation of Co and Cr clusters would

Table IV. Composition of the γ Precipitates from APT (Atomic Percent)

Phase	Secondary γ Precipitates	
Aging Time (h)	850 °C, 4 h	850 °C, 50 h
Ni	32.55 ± 1.62	42.98 ± 2.30
Cr	35.12 ± 1.74	23.60 ± 2.21
Al	1.13 ± 0.22	2.67 ± 0.63
Mo	2.03 ± 0.06	1.98 ± 0.30
B	0.01 ± 0.00	0.01 ± 0.00
Co	27.01 ± 0.35	25.68 ± 0.01
Nb	1.25 ± 0.24	1.98 ± 0.00
Ta	0.19 ± 0.05	0.27 ± 0.01
W	0.54 ± 0.01	0.69 ± 0.93

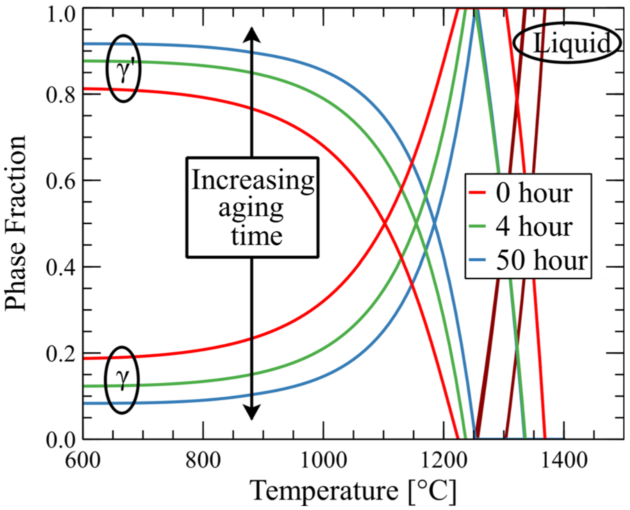

Fig. 6—Phase fraction plots as a function of aging time, calculated with Thermo-Calc using the APT γ' phase composition.

alleviate the supersaturation in the secondary γ' precipitates at the expense of interfacial energy from the newly formed surfaces. As these precipitates coarsen, the increasing interfacial energy contributes to the precipitate splitting, as a splitting event would result in redissolving of the secondary γ precipitates and an overall reduction in free energy resulting from changes in the interfacial and misfit strain energy.

As alloys become more complex, the theories governing their behavior should also increase in complexity as models based on simple systems start to deviate from reality. Modeling precipitate coarsening is important in predicting the behavior of superalloys; however, theories need to be modified to take into account not only the interfacial energy, but also the elastic strain energy, precipitate interaction energy, and the chemical energy. The phenomena of "inverse coarsening" or precipitate splitting was studied by many groups, and each alloy case seems to be different in terms of the mechanism governing the splitting. In RRHT1, it seems that a combination of bulk strain energy, local chemistry deviation of the γ matrix adjacent to the precipitate/matrix interface, and formation of γ precipitates contributes to the cyclic splitting behavior of the precipitates. As the refractory content in modern superalloys increases, due to the slow diffusion kinetics and large atomic sizes of the elements, more complex mechanisms governing their coarsening behavior will become apparent. In such cases, minor contributions from higher-order interactions will have to be taken into account, as they may become significant and impact the governing physics.

V. CONCLUSIONS

The conclusions based on the observations of the microstructural, chemical, and lattice evolution of the powder-processed, polycrystalline superalloy are as follows:

1. High-refractory content Ni-base superalloys undergo compositional, lattice, and morphological changes during aging at 1123 K (850 °C), even after slow cooling rates from the supersolvus heat treatment. Morphological instabilities result in phase separation in the form of finely dispersed particles in both the γ and γ' phases, even after near-equilibrium γ' volume fractions and phase compositions are attained during the aging.
2. Even though the bulk lattice parameters of the phases evolved during aging—increasing the lattice misfit, the evolution alone was not enough to cause a strain-induced morphological change. Local compositional differences in a ~ 5-nm matrix region adjacent to the γ/γ' interface, likely due to solute rejection from a growing γ', caused a significant increase in the lattice misfit.
3. Combined with the lattice misfit–driven surface instabilities, grooving and growth of nodes caused by the growth and coalescence of nanoscale γ precipitates serve to drive precipitate splitting during aging. These nanoscale γ precipitates formed as Cr and Co are rejected by the $L1_2$ structure; however, the diffusion distance to the matrix is too great.
4. Models for coarsening behavior of γ' precipitates need to be modified to take into account not only minimization of surface energy, but also chemical and elastic strain energy for modern superalloys with high-refractory contents and complex chemistries.

ACKNOWLEDGMENTS

The financial support for this investigation was provided by Rolls-Royce Corporation. The authors thank Saul Lapidus for the help with the synchrotron setup and Dieter Isheim for the useful discussion on the atom probe data. Additionally, use of the Advanced Photon Source at Argonne National Laboratory was supported by the United States Department of Energy, Office of Science, Office of Basic Energy Sciences, under Contract No. DE-AC02-06CH11357.

REFERENCES

1. C.T. Sims and W.C. Hagel: *Superalloys: Science & Technology of Materials*, Wiley, Hoboken, NJ, 1973.
2. R.F. Decker and C.T. Sims: *The Metallurgy of Nickel-Base Superalloys*, Paul D. Merica Research Laboratory, New York, 1972.
3. R.R. Unocic, G.B. Viswanathan, P.M. Sarosi, S. Karthikeyan, J. Li, and M.J. Mills: *Mater. Sci. Eng. A*, 2008, vols. 483–484, pp. 25–32.
4. D. Locq, P. Caron, S. Raujol, F. Pettinari-Sturmel, A. Coujou, and N. Clement: *Superalloys 2004 (10th Int. Symp.)*, TMS, Warrendale, PA, 2004, pp. 179–87.
5. T.M. Pollock and S. Tin: *J. Propuls. Power*, 2006, vol. 22, pp. 361–74.
6. D. Furrer and H. Fecht: *JOM*, 1999, vol. 51, pp. 14–17.

7. R.R. Unocic, L. Kovarik, C. Shen, P.M. Sarosi, Y. Wang, J. Li, S. Ghosh, and M.J. Mills: *Superalloys 2008 (11th Int. Symp.)*, TMS, Warrendale, PA, 2008, pp. 377–85.
8. R.C. Reed: *The Superalloys Fundamentals and Applications*, Cambridge University Press, Cambridge, UK, 2006.
9. G.W. Meetham: *Met. Technol.*, 1984, vol. 11, pp. 414–18.
10. M.J. Donachie and S.J. Donachie: *Superalloys: A Technical Guide*, 2nd ed., ASM International, Materials Park, OH, 2002.
11. S. Antonov, M. Detrois, R.C. Helmink, and S. Tin: *J. Alloys Compd.*, 2015, vol. 626, pp. 76–86.
12. T.M. Pollock and R.D. Field: *Dislocat. Solids*, 2002, vol. 11, pp. 547–618.
13. K.V. Vamsi and S. Karthikeyan: *MATEC Web Conf.*, 2014, vol. 14, p. 11005.
14. R.W. Kozar, A. Suzuki, W.W. Milligan, J.J. Schirra, M.F. Savage, and T.M. Pollock: *Metall. Mater. Trans. A*, 2009, vol. 40A, pp. 1588–1603.
15. H.A. Roth, C.L. Davis, and R.C. Thomson: *Metall. Mater. Trans. A*, 1997, vol. 28A, pp. 1329–35.
16. S. Antonov, M. Detrois, D. Isheim, D.N. Seidman, R.C. Helmink, R.L. Goetz, E. Sun, and S. Tin: *Mater. Des.*, 2015, vol. 86, pp. 649–55.
17. P.M. Mignanelli, N.G. Jones, K.M. Perkins, M.C. Hardy, and H.J. Stone: *Mater. Sci. Eng. A*, 2015, vol. 621, pp. 265–71.
18. M. Detrois, R.C. Helmink, and S. Tin: *Metall. Mater. Trans. A*, 2014, vol. 45A, pp. 5332–43.
19. M. Detrois, S. Antonov, R.C. Helmink, and S. Tin: *JOM*, 2014, vol. 66, pp. 2478–85.
20. S. Antonov, J. Huo, Q. Feng, D. Isheim, D.N. Seidman, R.C. Helmink, E. Sun, and S. Tin: *Mater. Sci. Eng. A*, 2017, vol. 687, pp. 232–40.
21. W. Ostwald: *Z. Phys. Chemie*, 1901, vol. 37, p. 385.
22. I.M. Lifshitz and V.V. Slyozov: *J. Phys. Chem. Solids*, 1961, vol. 19, pp. 35–50.
23. C. Wagner: *Z. Elektrochem.*, 1961, vol. 65, pp. 581–91.
24. A.J. Ardell: *Acta Metall.*, 1972, vol. 20, pp. 61–71.
25. P. Cha, D. Yeon, and S. Chung: *Scripta Mater.*, 2005, vol. 52, pp. 1241–45.
26. M. Doi, and T. Miyazaki: *Superalloys 1984 (5th Int. Symp.)*, TMS, Warrendale, PA, 1984, vol. 67, pp. 543–52.
27. M. Doi, T. Miyazaki, and T. Wakatsuki: *Mater. Sci. Eng.*, 1984, vol. 67, pp. 247–53.
28. M. Doi, T. Miyazaki, and T. Wakatsuki: *Mater. Sci. Eng.*, 1985, vol. 74, pp. 139–45.
29. T. Miyazaki, H. Imamura, and T. Kozakai: *Mater. Sci. Eng.*, 1982, vol. 54, pp. 9–15.
30. F. Vogel, N. Wanderka, Z. Balogh, M. Ibrahim, P. Stender, G. Schmitz, and J. Banhart: *Nat. Commun.*, 2013, vol. 4, p. 2955.
31. M. Doi, D. Miki, T. Moritani, and T. Kozakai: *Superalloys 2004 (10th Int. Symp.)*, TMS, Warrendale, PA, 2004, pp. 109–14.
32. S. Behrouzghaemi and R.J. Mitchell: *Mater. Sci. Eng. A*, 2008, vol. 498, pp. 266–71.
33. R.J. Mitchell, M. Preuss, M.C. Hardy, and S. Tin: *Mater. Sci. Eng. A*, 2006, vol. 423, pp. 282–91.
34. R.J. Mitchell, M. Preuss, S. Tin, and M.C. Hardy: *Mater. Sci. Eng. A*, 2008, vol. 473, pp. 158–65.
35. R.J. Mitchell and M. Preuss: *Metall. Mater. Trans. A*, 2007, vol. 38A, pp. 615–27.
36. S. Antonov, J. Huo, Q. Feng, D. Isheim, D.N. Seidman, R.C. Helmink, E. Sun, and S. Tin: *Scripta Mater.*, 2017, vol. 138, pp. 35–38.
37. S. Antonov, J. Huo, Q. Feng, D. Isheim, D.N. Seidman, E. Sun, and S. Tin: *Metall. Mater. Trans. A*, 2018, vol. 49A, pp. 729–39.
38. S. Antonov, W. Chen, J. Huo, Q. Feng, D. Isheim, D.N. Seidman, E. Sun, and S. Tin: *Metall. Mater. Trans. A*, 2018, vol. 49A, pp. 2340–51.
39. P.L. Lee, D. Shu, M. Ramanathan, C. Preissner, J. Wang, M.A. Beno, R.B. Von Dreele, L. Ribaud, C. Kurtz, S.M. Antao, X. Jiao, and B.H. Toby: *J. Synchrotron Radiat.*, 2008, vol. 15, pp. 427–32.
40. S. Antonov, D. Isheim, D.N. Seidman, E. Sun, R.C. Helmink, and S. Tin: *Proc. Int. Symp. on Superalloys*, 2016, vol. 2016.
41. Y. Mishima, S. Ochiai, and T. Suzuki: *Acta Metall.*, 1985, vol. 33, pp. 1161–69.
42. T.M. Pollock and A.S. Argon: *Acta Metall. Mater.*, 1992, vol. 40, pp. 1–30.
43. E. Nembach and G. Neite: *Prog. Mater. Sci.*, 1985, vol. 29 (3), pp. 177–319, https://doi.org/10.1016/0079-6425(85)90001-5.
44. N. Saunders, A.P. Miodownik, and J.-P. Schillé: *J. Mater. Sci.*, 2004, vol. 39, pp. 7237–43.
45. D.M. Collins, D.J. Crudden, E. Alabort, T. Connolley, and R.C. Reed: *Acta Mater.*, 2015, vol. 94, pp. 244–56.
46. A.G. Khachaturyan and V.M. Airapetyan: *Phys. Status Solidi*, 1974, vol. 26, pp. 61–70.
47. A.G. Khachaturyan, S.V. Semenovskaya, and J.W. Morris: *Acta Metall.*, 1988, vol. 36, pp. 1563–72.
48. A. Hazotte, T. Grosdidier, and S. Denis: *Scripta Mater.*, 1996, vol. 34, pp. 601–08.
49. Y. Chen, R. Prasath Babu, T.J.A. Slater, M. Bai, R. Mitchell, O. Ciuca, M. Preuss, and S.J. Haigh: *Acta Mater.*, 2016, vol. 110, pp. 295–305.
50. D.M. Collins, L. Yan, E.A. Marquis, L.D. Connor, J.J. Ciardiello, A.D. Evans, and H.J. Stone: *Acta Mater.*, 2013, vol. 61, pp. 7791–7804.
51. M.T. Lapington, D.J. Crudden, R.C. Reed, M.P. Moody, and P.A.J. Bagot: *Metall. Mater. Trans. A*, 2018, vol. 49A, pp. 2302–10, https://doi.org/10.1007/s11661-018-4558-7.